ZAMM - Journal of Applied Mathematics and Mechanics

ORIGINAL PAPER

Numerical Analysis of Nanofluid Flow Over Rotating Disk With Heat Source/Sink and Activation Energy

U. S. Mahabaleshwar[1] | K. M. Nagarathna[1] | K. M. Nihaal[1] | L. M. Pérez[2]

[1]Department of Studies in Mathematics, Davangere University, Shivagangothri, Davangere, India | [2]Departamento De Ingeniería Industrial y De Sistemas, Universidad De Tarapacá, Arica, Chile

Correspondence: U. S. Mahabaleshwar (u.s.m@davangereuniversity.ac.in) | K. M. Nihaal (nihaal.kmdvg@gmail.com)

Received: 18 January 2026 | **Revised:** 28 April 2026 | **Accepted:** 4 May 2026

Keywords: activation energy | heat source/sink | horizontal magnetic field | nanofluid | rotating disk

ABSTRACT

Considering the significance of disk-shaped geometries in various thermal and mass transfer based industrial systems such as automobile braking, fluid stirring in laboratories, and gas turbine engines, the present work aims to study the impact of horizontal magnetic field, heat source/sink, and activation energy over rotating disk. The mathematical model takes into the account the aggregation of nanoparticle for this analysis. The analysis is carried out in two different scenarios which is with nanoparticle aggregation and without nanoparticle aggregation. The numerical solution for this model is obtained via boundary value problem-5th collocation (bvp-5c) technique. Then the solutions are discussed via graphical plots. The significant outcomes reveal that both radial and tangential velocity profiles rise for stretching rate parameter but reduces for magnetic field parameter. Thermal analysis shows that the Biot number and heat sink/source enhance strength of temperature field, showcasing that the heat is penetrated more effectively. Rise in reaction rate causes concentration profile to drop whereas growing activation energy boosts concentration profile, highlighting regulated mass diffusion. The results from this study can optimize heat and mass transmission in rotating thermal applications like rotating heat exchangers, magnetic regulated energy reactors, and many more.

1 | Introduction

In many thermal applications, incorporating nanofluids, such as heat exchangers, improve heat transmission instead of traditional fluids. Thermophysical properties, especially heat conductivity is greatly affected by these nanofluids, making it significantly useful in industrial applications requiring better heat performance. Using nanofluids has been of great help to the advancement of research and development in the field of engineering. Several researchers have been studying mechanical and thermal characteristics of the nanofluid using several models [1–3]. Nihaal et al. [4] investigated the impact of thermophoresis and Brownian motion on moving thin needle in the presence/absence of nanoparticle aggregation. The results reveal that rise in thermal and concentration profile for Brownian are great in case of without

Abbreviations: MHD, magneto hydro dynamics; C-C, Cattaneo–Christov; bvp-5c, boundary value problem fifth collocation; PDE, partial differential equation; RKF, Runge–Kutta–Felhberg; IVP, initial value problem; BVP, boundary value problem.

nanoparticle aggregation. Waseem et al. [5] conducted a comparative examination of the impact of MHD, heat source/sink, and activation energy on micro-polar and second-grade nanofluid fluid over permeable three-dimensional exponential stretching sheet. Considering Buongiorno and Darcy medium model, Batti et al. [6] scrutinized the MHD convective nanofluid flow past a spinning disk. Sarfaraz et al. [7] explored the impact of different type of nanoparticles on stagnation point flow across stretching surface. The results show that hybrid nanofluids perform better than mono nanofluids in flow and heat transfer properties.

Magnetohydrodynamics (MHD) describes the relationship between a fluid that conducts electricity and a magnetic field. The magnetic field is often believed to act perpendicular to the flow in all MHD models. Muhammad and Sarfaraz [8] examined the influence of MHD on hybrid nanofluid flow across a permeable parallel plates in the presence of Darcy–Forchhiemer model. The influence of nonlinear radiation and variable thermal conductivity on MHD hybrid nanofluid flow across a spinning disk was investigated by Mandal et al. [9]. Conversely, there has been very little research on using a horizontal MHD. In context to horizontal MHD, the components of the Lorentz force undergo considerable alteration due to the modified interaction between the induced current and field. This results in varied influence on axial, radial, tangential velocity components depending on the flow geometry. The role of horizontal magnetic field on fluid flow and heat transmission across a revolving disk was shown by Turkyilmazoglu's [10] novel research on horizontal MHD. The impact of horizontal MHD and activation energy on radio-active nanofluid flow across a rotating disk was studied by Shehzad et al. [11]. Pandey and Das [12] scrutinized hybrid nanofluid flow across a spinning disk in the presence of horizontal MHD and exponential heat sink/source with Cattaneo–Christov model.

Heat source/sink is an additional term added to the energy equation indicating an energy balance or heat conduction. Heat source is responsible for temperature rise and heat sink is responsible for reduction in temperature. Awais et al. [13] examined MHD fluid flow on a rotating disk due to the impact of heat source/sink and chemical reaction. The study reveals that fluid temperature elevates for augmented values of heat generation while decreasing for augmented values of heat absorption parameters. Kumar and Sharma [14] studied the impact of the heat sink/source on fluid flow over a moving stretched rotating disk with Darcy–Forchheimer medium. The rate of heat transfer is found to be rising for stretching parameter while decreases for heat source parameter. Sarfaraz et al. [15] obtained numerical solutions of the impact of heat source/sink over a nanofluid flow of Walter's B fluid across a shrinking/stretching surface. Nihaal et al. [16] examined the effects of activation energy and exponential heat sink/source on ternary nanofluid bioconvective flow over an extending disk. Farooq et al. [17] analyzed the behavior of radioactive hybrid nanofluid flow under the influence of permeable rotating disk. The findings demonstrate that fluid temperature rises for growing heat sink/source parameter.

A minimal amount of energy necessary to initiate a certain reaction or mechanical process is referred as activation energy. It serves as an energy resistance that reactant molecules must overcome in order to reach the high energy transition state before converting into products. Arafat et al. [18] examined the consequence of activation energy on bioconvective nanofluid flow past a rotating disk considering entropy production. The numerical study on Maxwell nanofluid considering the impacts of activation energy and entropy generation over a spinning disk was analyzed by Alsallami et al. [19]. Paul et al. [20] investigated the consequences of porous medium and activation energy over chemically reactive Casson ternary nanofluid flow across a spinning disk. Khouqeer et al. [21] investigated MHD ternary nanofluid flow across a rotating disk in the presence of thermal radiation and activation energy. Asma et al. [22] explored MHD nanofluid flow pass though rotating disk with the thermophoresis and Brownian motion, and activation energy.

Mohanty et al. [23] explored Joule heating and radiation phenomenon on Darcy–Forchheimer imposed ternary nanofluid flow across rotating disk. Upon considering dissipation and C–C heat flux model, Tulu et al. [24] studied unsteady hybrid nanofluid flow across a spinning disk in the presence of MHD. Taking into account of variable thermal conductivity and chemical reaction, Meena and Sharma [25] explored heat and mass transfer analysis on radioactive hybrid nanofluid flow past a rotating disk. Using response surface methodology, Jalili et al. [26] examined the heat transfer of nanofluid flow over a spinning disk in the presence of MHD and radiation. Taking into account C–C heat flux model and bioconvective phenomenon, Galal et al. [27] studied chemically reactive ternary nanofluid flow across an inclined rotating disk due to impacts of radiation. The analysis of flow and heat transfer properties of nanofluid flow across disks under the influence of MHD, convective boundary conditions, and radiation is found in these studies [28–30].

1.1 | Novelty

The current study presents a unique comparison of convective nanofluid flow across a stretched rotating disk incorporating nanoparticle aggregation and non-aggregation effects in the presence of horizontal MHD, which varies significantly from traditional vertical MHD models. Previous studies have mostly focused on standard vertical MHD, heat sink/source, and chemical reaction on rotating disk separately, ignoring the synergetic effects that arise from combined influence

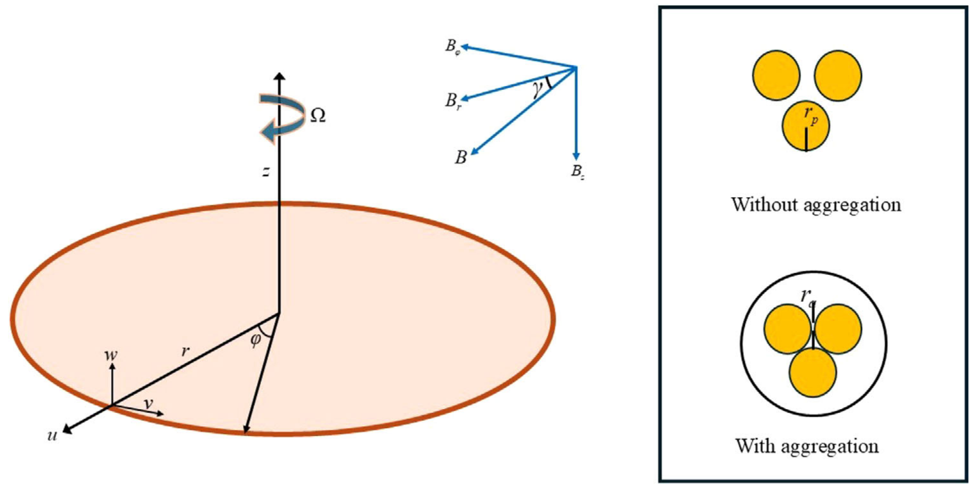

FIGURE 1 | Schematic representation of problem.

of horizontal magnetic field, heat source/sink, activation energy, convective boundary conditions, and aggregation of nanoparticles. It is evident from the current literature that the comparative analysis of nanofluid flow over a rotating disk with/without nanoparticle aggregation has been unexplored. Additionally, nanoparticle aggregation has a significant influence on temperature and concentration boundary layers by altering thermophysical properties and effective transport characteristics. Further, the problem is demonstrated via governing PDE model and solution is obtained numerically through bvp-5c algorithm. The result from this study offers design oriented insights for maximizing heat and mass transfer in rotating thermal systems, the research also assesses important engineering factors like Nusselt number and Sherwood number.

1.2 | Mathematical Formulation

The present study incorporates a laminar, incompressible nanofluid flow across a rotating disk. The surface of the disk stretches at a constant rate c radially along r. The swirl flow over the surface is caused due to the rotation of disk with constant angular velocity Ω. The horizontal MHD is applied to the disk with magnetic field strength B. With a cylindrical coordinate $\{r, \varphi, z\}$, the respective velocities considered are $\{u, v, w\}$. An aggregation of TiO_2 nanoparticles is considered in nanofluid flow (see Figure 1). Further, heat source/sink and activation energy are considered to examine the thermal and concentration profiles, and the surface is subjected to convective boundary condition.

In cylindrical coordinates, using uniform magnetic field $\vec{B}$ and $\vec{J}$, Lorentz force can be defined as follows [10]:

$$\vec{J} \times \vec{B} = \sigma_e \left(\vec{V} \times \vec{B} \right) \times \vec{B}, \tag{1}$$

The aforementioned Equation (1) can be simplified down into component form as follows:

$$\vec{J} \times \vec{B} = \sigma_e \begin{pmatrix} B_z \{B_r w - B_z u\} + B_\varphi \{B_r v - B_\varphi u\}, \\ B_z \{B_\varphi w - B_z v\} + B_r \{B_\varphi u - B_r v\}, \\ B_\varphi \{B_\varphi w - B_z v\} + B_r \{B_z u - B_r w\}, \end{pmatrix}, \tag{2}$$

Similarity solutions can be derived only when the magnetic field configuration preserves axial symmetry. Hence, the following condition is considered.

$$B_r = B_\varphi = 0, \tag{3}$$

Using this condition, the equation is converted to this form:

$$\vec{J} \times \vec{B} = \sigma_e B_z^2 (-u, -v, 0). \tag{4}$$

Other than Equation (3), at $B_z = 0$, another similarity is a possibility.

$$\vec{J} \times \vec{B} = \sigma_e \begin{pmatrix} B_\varphi \left\{ B_r v - B_\varphi u \right\}, \\ B_r \left\{ B_\varphi u - B_r v \right\}, \\ \left\{ B_\varphi^2 + B_r^2 \right\} w. \end{pmatrix}. \tag{5}$$

The angle of inclination between the radial direction and the magnetic field $\vec{B}$ (along $B_z = 0$) is denoted by γ. Then components of magnetic field $\vec{B} = (B_r, B_\varphi, 0)$ can be derived as follows:

$$B_r = |B| \cos\gamma,\ B_\varphi = |B|\ \mathrm{Sin}\gamma. \tag{6}$$

Considering Equation (6), the reduced form of equation can be written as,

$$\vec{J} \times \vec{B} = \sigma_e \begin{pmatrix} |B|\ \mathrm{Sin}\gamma \left(|B|\ \mathrm{Cos}\gamma v - |B|\ \mathrm{Sin}\gamma u \right), \\ |B|\ \mathrm{Cos}\gamma \left(|B|\ \mathrm{Sin}\gamma u - |B|\ \mathrm{Cos}\gamma v \right), \\ -|B|^2 w. \end{pmatrix}. \tag{7}$$

By taking into the account of above-mentioned considerations, the governing model is derived as follows see ([10, 15, 17, 22]):

$$\frac{u}{r} + \frac{\partial u}{\partial r} + \frac{\partial w}{\partial z} = 0, \tag{8}$$

$$\frac{v^2}{r} + u\frac{\partial u}{\partial r} + w\frac{\partial u}{\partial z} + \frac{1}{\rho_{nf}}\frac{\partial p}{\partial r} = v_{nf}\left\{ -\frac{u}{r^2} + \frac{1}{r}\frac{\partial u}{\partial r} + \frac{\partial^2 u}{\partial r^2} + \frac{\partial^2 u}{\partial z^2} \right\} + \frac{\sigma_e}{\rho_{nf}}\left\{ |B|\ \mathrm{Sin}\gamma \left(v\,|B|\ \mathrm{Cos}\gamma - u\,|B|\ \mathrm{Sin}\gamma \right) \right\}, \tag{9}$$

$$\frac{uv}{r} + u\frac{\partial v}{\partial r} + w\frac{\partial v}{\partial z} = v_{nf}\left\{ -\frac{v}{r^2} + \frac{1}{r}\frac{\partial v}{\partial r} + \frac{\partial^2 v}{\partial r^2} + \frac{\partial^2 v}{\partial z^2} \right\} + \frac{\sigma_e}{\rho_{nf}}\left\{ |B|\ \mathrm{Cos}\gamma \left(u\,|B|\ \mathrm{Cos}\gamma - v\,|B|\ \mathrm{Sin}\gamma \right) \right\}, \tag{10}$$

$$u\frac{\partial w}{\partial r} + w\frac{\partial w}{\partial r} + \frac{1}{\rho_{nf}}\frac{\partial p}{\partial z} = v_{nf}\left(\frac{\partial^2 w}{\partial r^2} + \frac{1}{r}\frac{\partial w}{\partial r} + \frac{\partial^2 w}{\partial z^2} \right) - \left(\frac{1}{\rho_{nf}} \right)|B|^2 w, \tag{11}$$

$$u\frac{\partial T}{\partial r} + w\frac{\partial T}{\partial z} = \frac{k_{nf}}{(\rho Cp)_{nf}}\left(\frac{\partial^2 T}{\partial r^2} + \frac{1}{r}\frac{\partial T}{\partial r} + \frac{\partial^2 T}{\partial z^2} \right) + \frac{Q_0}{(\rho Cp)_{nf}}\left(T - T_\infty \right), \tag{12}$$

$$u\frac{\partial C}{\partial r} + w\frac{\partial C}{\partial z} = D\left(\frac{\partial^2 C}{\partial r^2} + \frac{1}{r}\frac{\partial C}{\partial r} + \frac{\partial^2 C}{\partial z^2} \right) - K_r^*\left(C - C_\infty \right)\left\{ \frac{T}{T_\infty} \right\}^n e^{-(E_a/KT)}, \tag{13}$$

where, v—kinematic viscosity, ρ—density, σ_e—magnetic conductivity, p—pressure term, k—thermal conductivity, Cp—specific heat capacity, Q_0—volumetric rate of heat source/sink, D—diffusivity, K_r^*—reaction rate, $\{T/T_\infty\}^n e^{-(E_a/KT)}$—modified Arrhenius function. The corresponding boundary conditions and proper similarities are as follows:

$$u = cr,\ \ v = 0, = k_{nf}\frac{\partial T}{\partial z} = h_f\left(T_w - T \right),\ \ C = C_w\ \ at\ \ z = 0, \tag{14}$$

$$\frac{\partial u}{\partial z} \to 0,\ \ v = \Omega r,\ T \to T_\infty,\ \ C \to C_\infty\ \ as\, z \to \infty. \tag{15}$$

TABLE 1 | Thermo-physical characteristics of nanofluid and base fluid [4].

Particles	Thermal conductivity	Density	Heat capacitance
TiO_2	8.9538	4250	686.2
Eg	0.252	1114	2415

and

$$\eta = z\sqrt{\frac{\Omega}{\nu_f}}, u = \Omega rF(\eta), v = \Omega r G(\eta), w = \sqrt{\Omega v_f}H(\eta), \tag{16}$$

$$p = \rho_f v_f \Omega \mathrm{P}(\eta), \theta(\eta) = \frac{T - T_\infty}{T_w - T_\infty}, \chi(\eta) = \frac{C - C_\infty}{C_w - C_\infty}. \tag{17}$$

Here, (nf, f)—nanofluid and base fluid subscripts, h_f—convective heat transfer coefficient, (T_w, T_∞) and (C_w, C_∞)—temperature and concentration at surface and far field from surface respectively. Table 1 displays the thermophysical properties of nanofluid and base fluid.

Here are the correlations for the characteristics of the nanofluid when aggregations of nanoparticles are considered [31].

$$\mu_{nf} = \mu_f\left(1 - \phi_{agg}\phi_{\max}^{-1}\right)^{-\phi\max 2.5}, \tag{18}$$

$$\rho_{nf} = \phi_{agg}\rho_{agg} + \left(1 - \phi_{agg}\right)\rho_f, \tag{19}$$

$$(\rho Cp)_{nf} = \phi_{agg}(\rho Cp)_{agg} + \left(1 - \phi_{agg}\right)(\rho Cp)_f, \tag{20}$$

$$k_{nf} = \frac{2k + k_{agg} + 2\phi_{agg}\left(k_{agg} - k_f\right)}{2k + k_{agg} - 2\phi_{agg}\left(k_{agg} - k_f\right)}k_f, \tag{21}$$

Physical properties are analyzed by these models in the framework of aggregation.

$$\rho_{agg} = \phi_{\text{int}}\rho_s + (1 - \phi_{\text{int}})\rho_f, \tag{22}$$

$$\phi_{agg} = \frac{\phi}{\phi_{\text{int}}}, \tag{23}$$

$$\phi_{\text{int}} = \left(\frac{R_{agg}}{R_p}\right)^{D-3}, \tag{24}$$

$$(\rho Cp)_{agg} = \phi_{\text{int}}(\rho Cp)_s + (1 - \phi_{\text{int}})(\rho Cp)_f. \tag{25}$$

$$k_{agg}=\frac{k_f}{4}\left\{\begin{array}{l}(3\phi_{int}-1)\frac{k_s}{k_f}+(3(1-\phi_{int})-1)\\+\left(\left((3\phi_{int}-1)\frac{k_s}{k_f}+(3(1-\phi_{int})-1)\right)^2+\frac{8k_s}{k_f}\right)^{1/2}\end{array}\right\}. \tag{26}$$

Using similarities (16-17), the Equations (8–15) are converted as reduced equations and boundary conditions follows:

$$2\mathrm{F}(\eta)+\mathrm{H}'(\eta)=0, \tag{27}$$

$$\frac{\upsilon_{nf}}{\upsilon_f}\mathrm{F}''(\eta)+\mathrm{G}(\eta)^2-\mathrm{F}(\eta)^2-\mathrm{H}(\eta)\mathrm{F}'(\eta)+\frac{1}{(\rho Cp)_{nf}/(\rho Cp)_f}M\sin\gamma(\mathrm{G}(\eta)\cos\gamma-\mathrm{F}(\eta)\sin\gamma)-1=0, \tag{28}$$

$$\frac{\upsilon_{nf}}{\upsilon_f}\mathrm{G}''(\eta)-2F(\eta)\mathrm{G}(\eta)-\mathrm{H}(\eta)\mathrm{G}'(\eta)+\frac{1}{(\rho Cp)_{nf}/(\rho Cp)_f}M\cos\gamma(\mathrm{F}(\eta)\sin\gamma-\mathrm{G}(\eta)\cos\gamma)=0, \tag{29}$$

$$\frac{1}{\Pr(\rho Cp)_{nf}/(\rho Cp)_f}\theta''(\eta)-\mathrm{H}(\eta)\theta'(\eta)+\frac{Q}{(\rho Cp)_{nf}/(\rho Cp)_f}\theta(\eta)=0, \tag{30}$$

$$\frac{1}{Sc}\chi''(\eta)-\mathrm{H}(\eta)\chi'(\eta)-Rc\chi(\eta)(1+\delta\theta(\eta))^n e^{-E/(1+\delta\theta(\eta))}=0. \tag{31}$$

and

$$\text{at } \eta=0:\ \mathrm{F}(0)=S,\ \mathrm{G}(0)=0,\ \mathrm{H}(0)=0,\ \theta'(\eta)=-Bi^*(1-\theta(\eta)),\ \chi(0)=1, \tag{32}$$

$$\text{as. } \eta\to\infty:\ \mathrm{F}'(\eta)\to 0,\ \mathrm{G}(\eta)=1,\ \theta(\eta)=0,\ \chi(\eta)=0 \tag{33}$$

where,

$M=\frac{\sigma_e B^2}{\rho_f\Omega}$, $Q=\frac{Q_0}{(\rho Cp)_f\Omega}$, $Sc=\frac{\upsilon_f}{D}$, $Rc=\frac{K_r^*}{\Omega}$, $Bi^*=\frac{h_f}{k_f}\sqrt{\frac{\upsilon_f}{\Omega}}$, $S=\frac{c}{\Omega}$, $\delta=\frac{T_w}{T_\infty}$, $E=\frac{E_a}{KT_\infty}$ are magnetic field, heat source/sink, Schmidt number, chemical reaction parameter, Biot number, stretching ratio parameter, temperature difference ratio, and activation energy parameter.

From Equation (11), we obtain,

$$\frac{\upsilon_{nf}}{\upsilon_f}\mathrm{H}''(\eta)-\mathrm{H}(\eta)\mathrm{H}'(\eta)-P'(\eta)-\frac{1}{\rho_{nf}/\rho_f}\mathrm{MH}(\eta)=0, \tag{34}$$

From above equation, the pressure term is derived as follows:

$$\mathrm{P}(\eta)=\mathrm{H}'(\eta)-\frac{H(\eta)^2}{2}-M\int_0^\infty \mathrm{H}(\eta)\,d\eta\,. \tag{35}$$

Engineering factors with their reduced form.

Skin friction: $Cf = \frac{(\tau_r^2+\tau_\theta^2)^{1/2}}{\rho_f (r\Omega)^2}, \tau_r = \mu_{nf}(\frac{\partial u}{\partial z})|_{z=0}, \tau_\theta = \mu_{nf}(\frac{\partial v}{\partial z})|_{z=0}.$

$$Cf = \frac{1}{\mathrm{Re}}\left(\frac{\mu_{nf}}{\mu_f}\right)\sqrt{F'(0)^2 + G'(0)^2}. \tag{36}$$

Nusselt number: $Nu = \frac{rq_w}{k_f(T_w - T_\infty)}, q_w = -k_{nf}(\frac{\partial T}{\partial z})|_{z=0}.$

$$\mathrm{Re}^{-1/2} Nu = -\left(\frac{k_{nf}}{k_f}\right)\theta'(0). \tag{37}$$

Sherwood number: $Sh = \frac{rq_c}{D(C_w - C_\infty)}, q_c = -D\frac{\partial C}{\partial y}|_{z=0}.$

$$\mathrm{Re}^{-1/2} Sh = -\chi'(0). \tag{38}$$

1.3 | Numerical Methodology

The system of Equations (27–33) are highly stiff non-linear and highly order equations and thus it is highly hard to obtain closed-form solutions from such type of system of equations. Hence, shooting method and RKF-45$^{\mathrm{th}}$ approaches are used to obtain numerical solution. Initially, these high order equations are reduced to first order system of equations as follows:

$$\begin{Bmatrix} F(\eta) \\ F'(\eta) \\ F''(\eta) \\ G(\eta) \\ G'(\eta) \\ G''(\eta) \\ H(\eta) \\ H'(\eta) \\ H''(\eta) \end{Bmatrix} = \begin{Bmatrix} y(1) \\ y(2) \\ y(2)' \\ y(3) \\ y(4) \\ y(4)' \\ y(5) \\ y(6) \\ y(6)' \end{Bmatrix} and \begin{Bmatrix} \theta(\eta) \\ \theta'(\eta) \\ \theta''(\eta) \\ \chi(\eta) \\ \chi'(\eta) \\ \chi''(\eta) \end{Bmatrix} = \begin{Bmatrix} y(7) \\ y(8) \\ y(8)' \\ y(9) \\ y(10) \\ y(10)' \end{Bmatrix} \tag{39}$$

$$\mathrm{F}''(\eta) = -\left(\frac{1}{\upsilon_{nf}/\upsilon_f}\right)\left(y(3)^2 - y(1)^2 - y(5)y(2) + \frac{1}{(\rho Cp)_{nf}/(\rho Cp)_f} M\mathrm{Sin}\gamma\,(y(3)\,\mathrm{Cos}\gamma - y(1)\,\mathrm{Sin}\gamma) - 1\right), \tag{40}$$

$$G''(\eta) = -\left(1/\left(\upsilon_{nf}/\upsilon_f\right)\right)\left(-2y(1)y(3) - y(4)y(5) + \frac{1}{(\rho Cp)_{nf}/(\rho Cp)_f} M\mathrm{Cos}\gamma\,\{y(1)\mathrm{Sin}\gamma - y(3)\mathrm{Cos}\gamma\}\right), \tag{41}$$

$\mathrm{H}'(\eta) = -2y(1),$

$$\theta''(\eta) = -\left(\Pr(\rho Cp)_{nf}/(\rho Cp)_f\right)\left(-y(5)y(8) + \frac{Q}{(\rho Cp)_{nf}/(\rho Cp)_f} y(7)\right), \tag{42}$$

$$\chi''(\eta) = -Sc\left(-y(5)y(10) - Rcy(9)(1 + \delta y(7))^n e^{-E/(1+\delta y(7))}\right). \tag{43}$$

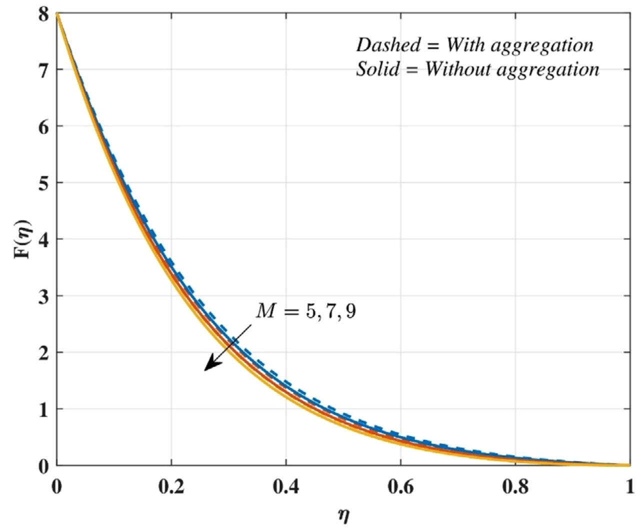

FIGURE 2 | Effect of M on $F(\eta)$.

and

$$at\,\eta = 0 : \; y(1) - S,\; y(3),\; y(5),\; y(8) = -Bi^{*}(1 - y(7)),\; y(9) - 1, \tag{44}$$

$$\text{as } \eta \to \infty : y(2) \to 0,\; y(3) - 1,\; y(7),\; y(9). \tag{45}$$

Then this BVP is reduced to IVP using suitable preliminary guesses. This IVP is then resolved via RKF-45$^{\text{th}}$ approach. For having precise numerical solutions, the convergence norm is considered to be 10^{-5} and step size $h = 0.01$.

2 | Results and Discussion

This section discusses the impact of certain parameters over fluid velocity, temperature, and concentration profiles on nanofluid flow over a rotating disk. Such parameters are horizontal magnetic field M, heat source/sink Q, chemical reaction Rc, Biot number Bi^{*}, stretching ratio S, temperature difference δ, and activation energy E. The nanofluid flow model is investigated in two diverse cases: with nanoparticle (Np) aggregation (agg) ($\phi_c \neq 1$) and without nanoparticle (Np) aggregation ($\phi_c = 1$). Also, engineering factors like Skin friction Cf, Nusselt number Nu, and Sherwood number are discussed for distinct values of certain parameters. Solutions in case of with nanoparticle agg are specified by dashed lines and without nanoparticle agg is specified by solid lines in the plots. The standard range of parameters for computational purposes are as follows: $1 \le M \le 9,\ 1 \le Q \le 2.5,\ 0.8 \le Rc \le 1.2,\ 7 \le Bi^{*} \le 9,\ 3 \le S \le 5,\ 0.4 \le \delta \le 1.0,\ 0.6 \le E \le 1.0,$ $\phi_c \neq 1$ and $\phi_c = 1$.

The effect of M on radial velocity $F(\eta)$ is shown in Figure 2. From figure, it can be observed that growing values of M decreases $F(\eta)$. Physically, rise in magnetic field develops Lorentz force, this develops a resisting force which causes fluid velocity to decline. From figure, it is found that the reduction is more in without Np agg case compared to with Np agg case due to less viscous force and resistance.

The effect of directional angle γ on $F(\eta)$ is displayed in Figure 3. A decreasing trend is observed in $F(\eta)$ for rising values of γ. Physically, as γ increases, the magnetic field component $B_{\varphi} = |B|Sin\gamma$ aligned in circumstantial direction becomes stronger. The interaction between this circumstantial magnetic field component B_{φ} and the radial flow velocity $F(\eta)$ induced Lorentz force. When angle γ reaches 90 degrees, the radial retarding force is maximized, effectively acting as a resistive force that significantly slows down radial movement of the electrically conducting fluid, thus causing the reduction in radial velocity profile. The drop is observed to be greater in without Np agg case when compared with Np agg case.

The impact of S over $F(\eta)$ is displayed in Figure 4. $F(\eta)$ increases for augmented values of S. Physically, as the stretching ratio parameter grows, the disk too extends radially, leading to increase in $F(\eta)$. The rise in $F(\eta)$ is greater for with Np agg when compared to without Np agg due to enhanced velocity transport.

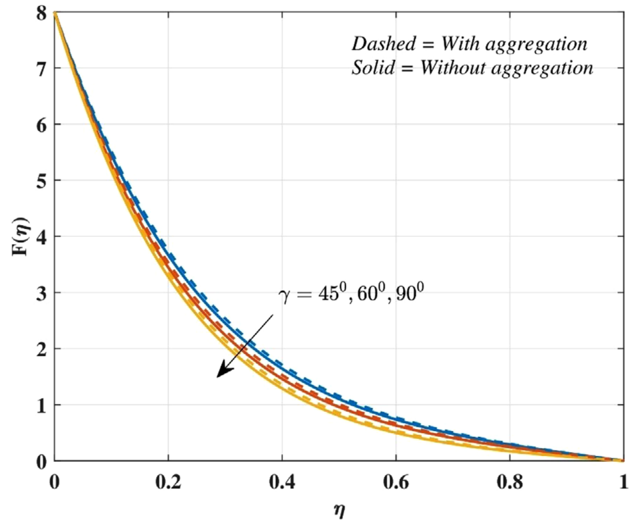

FIGURE 3 | Effect of γ on $F(\eta)$.

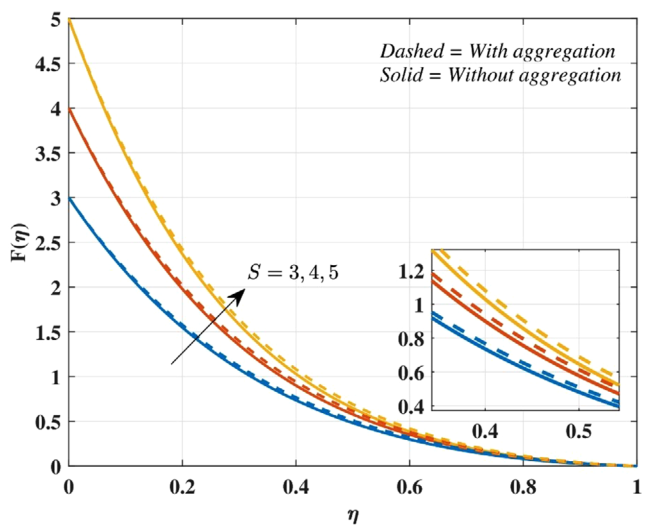

FIGURE 4 | Effect of S on $F(\eta)$.

The impact of M on tangential velocity $G(\eta)$ is depicted in Figure 5. Tangential velocity decreases for growing values of M. This is due to rising resistive force referred as Lorentz force created from rising magnetic field. Further, the reduction is greater in with Np agg compared to without Np agg due to enhanced interaction between electrical conductivity and Lorentz force.

Figure 6 displays the effect of direction angle γ on $G(\eta)$. From figure, it is evident that larger values of γ rises $G(\eta)$. Physically, as γ increases, the term $Cos\gamma$ reduces with rise in term $Sin\gamma$ making the magnetic term $M\cos\gamma(\mathrm{F}(\eta)\sin\gamma - \mathrm{G}(\eta)\cos\gamma)$ deteriorate its damping effect on tangential motion. With less magnetic effect, the tangential velocity $G(\eta)$ increases. Moreover, the rise is greater in without Np agg when compared with Np agg due to less magnetic damping.

Figure 7 shows that increasing nature of $G(\eta)$ under the effect of S. Physically, expanding the disk in the radial direction propels fluid particles outward, while the fluid gets extra azimuthal motion to conserve angular momentum. As a result, with growing stretching rates, the tangential velocity within the boundary layer increases. Also, this stretching minimizes the oscillating nature of the velocity profile. Further, the rise is greater in without Np agg case when compared with Np agg due to less resistance toward tangential motion.

Figure 8 displays the impact of S over axial velocity profile $H(\eta)$. From figure, augmentation in S reduces $H(\eta)$. Physically, to maintain continuity, the additional fluid is pulled downward toward the disk as it is moved outward over the disk surface. So, when the stretching increases, the axial velocity becomes more negative, which shows a reduction in the axial

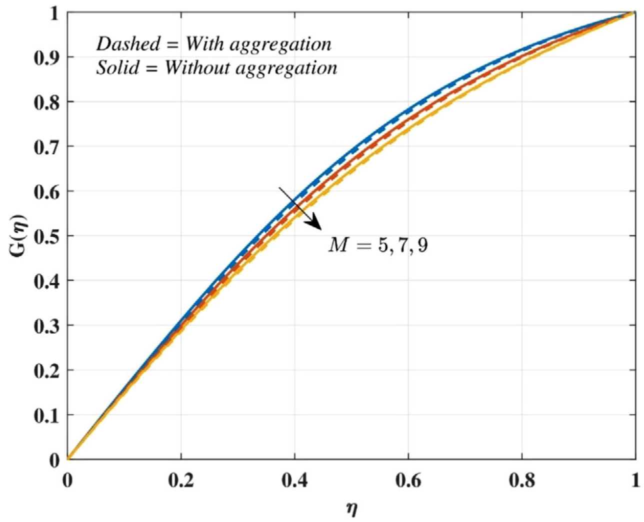

FIGURE 5 | Impact of M on $G(\eta)$.

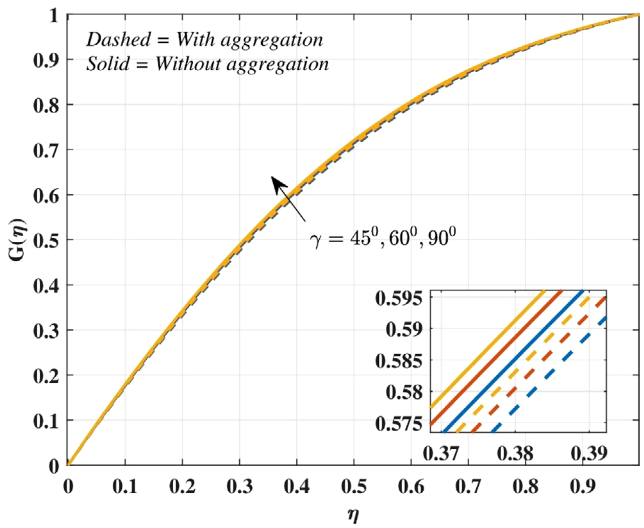

FIGURE 6 | Impact of γ on $G(\eta)$.

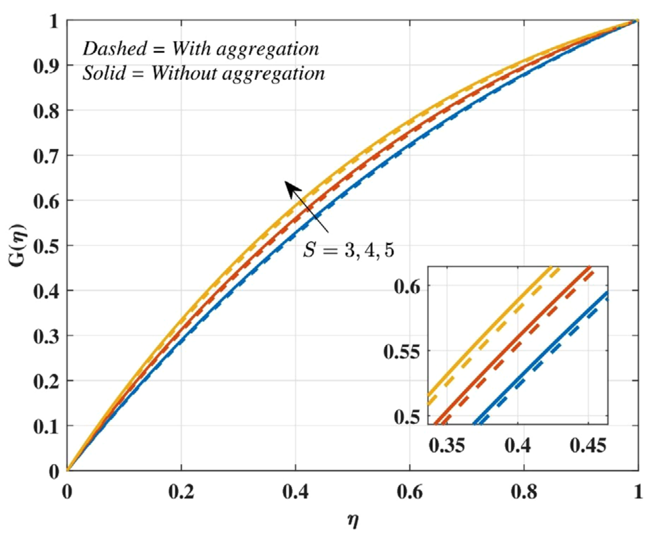

FIGURE 7 | Impact of S on $G(\eta)$.

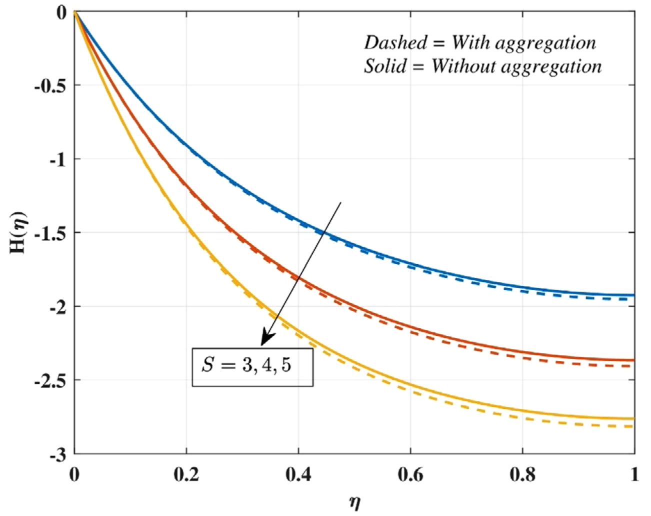

FIGURE 8 | Impact of S over $H(\eta)$.

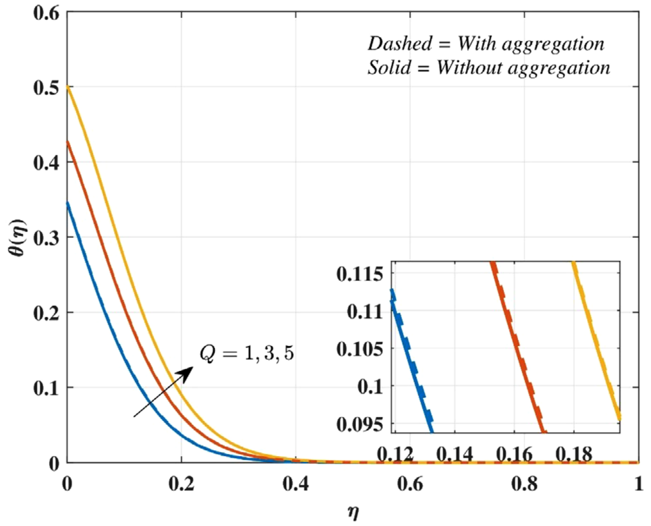

FIGURE 9 | Effect of Q on $\theta(\eta)$.

velocity profile. Further, the drop is observed greater with Np agg case when compared to without Np agg due to greater resistance toward axial motion.

The impact of heat source/sink Q and Biot number Bi^* on temperature profile $\theta(\eta)$ in Figures 9 and 10, respectively. It is seen that $\theta(\eta)$ increases for growing values of both Q and Bi^*. Physically, this is because an increase in heat source/sink and Biot number causes thermal field to become stronger, leading to a higher temperature within the fluid flow. Further, the greater rise is observed in with Np agg case when compared to without Np agg due to improved thermal conductivity.

The effect of chemical reaction parameter Rc over concentration profile $\chi(\eta)$ is depicted in Figure 11. A decreasing behavior is seen in $\chi(\eta)$ for increasing values of Rc. This is because, when Rc parameter is increased, the solute molecules in chemical reaction gets bigger which leads to less concentration in the fluid domain. Further, the decrease is found to be more in the case with Np agg compared to without Np agg due to increased diffusivity.

Figure 12 shows the increasing behavior of $\chi(\eta)$ under the effect of E. Physically, increasing activation energy leads to weakening of the Arrhenius function, which in turn accelerates chemical reaction and increases concentration of the fluid domain. Further, the rise is greater in without Np aggregation case when compared with Np agg due to less particle interaction and low mass diffusion resistance.

Figure 13 portrays the behavior of Cf for varying values of S and M. From figure, it is found that Cf for both rising values of M and S. Physically, growing values of magnetic field, the Lorentz force produced by the interaction of the applied magnetic field and electrically conducting fluid causes to rise. This force slows down fluid motion and results in steeper

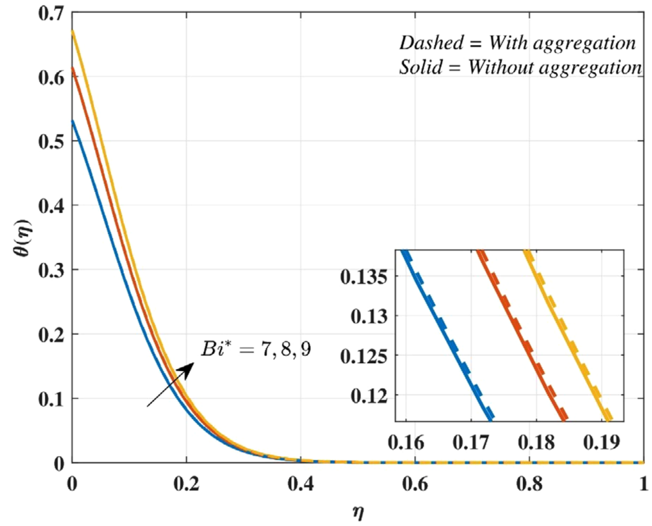

FIGURE 10 | Effect of Bi^* on $\theta(\eta)$.

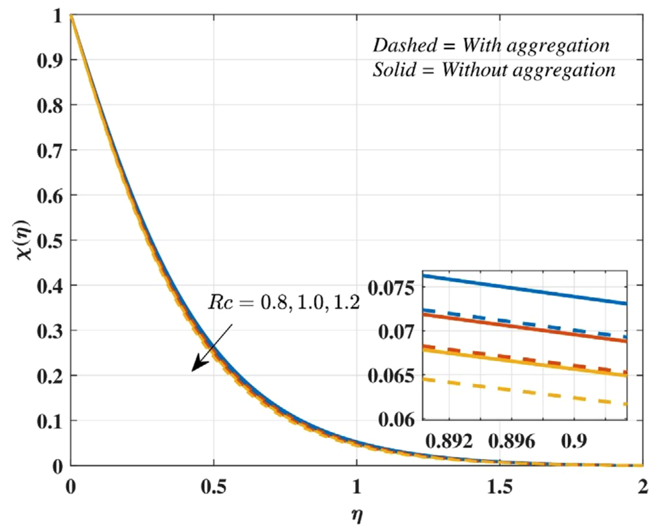

FIGURE 11 | Effect of Rc on $\chi(\eta)$.

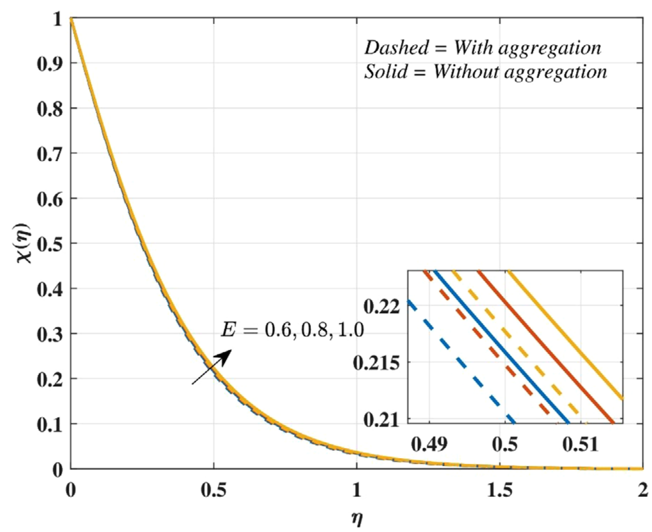

FIGURE 12 | Effect of E on $\chi(\eta)$.

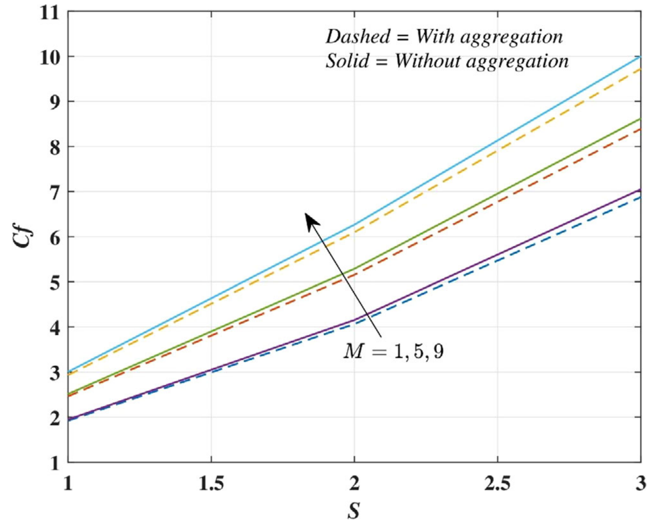

FIGURE 13 | Variation in Cf against M and S.

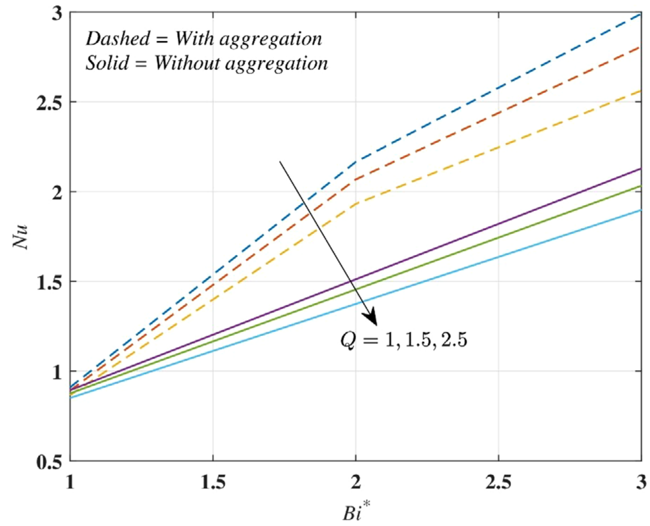

FIGURE 14 | Variation of Nu against Q and Bi^*.

velocity gradients near the surface. This leads to increase in wall shear stress and thereby rise in Cf. Also, larger values of stretching parameter makes the dragging force on the fluid more pronounced. The impact if observed to be greater in without Np agg compared to with Np agg due to small effective viscous force which causes steeper velocity gradients at the surface.

Figure 14 portrays the behavior of Nusselt number Nu under the influence of Q and Bi^*. From figure, it is seen that Nusselt number decreases for Q and increases for Bi^*. Physically, greater heat source/sink parameter makes the fluid more thermally active, increasing overall temperature within the fluid domain but decreases the temperature difference near the wall. Since Nusselt number is proportional to wall gradient temperature, it reduces. In contrast, increasing Biot number improves surface convective heat exchange strengthening heat transmission from wall to the fluid. This results in greater temperature gradients near the wall and thus rising Nusselt number. Further, due to less thermal conductivity, it is seen that reduction is greater in without Np agg.

The behavior of Sh under the influence of Rc and E is portrayed in Figure 15. From figure, it is seen that Sh increases for varying values of chemical reaction parameter and decreases for varying value of activation energy parameter. Physically, the solute molecules in chemical reaction get bigger upon increasing chemical reaction promoting more mass transfer whereas a slightly decrease in mass transfer is found upon increasing activation energy because only few solute molecules are able to cross the energy barrier produced by increasing activation energy. Also, due to improved effective diffusivity and mass transfer, the rise in greater in with Np agg.

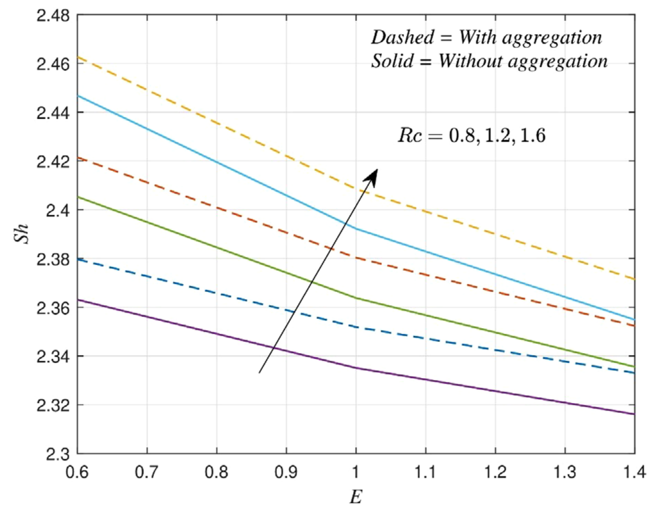

FIGURE 15 | Variation in Sh against Rc and E.

3 | Conclusion

This work has examined the influence of horizontal MHD, heat sink/source, and activation energy on nanofluid flow over a rotating disk subjected to convective boundary conditions. The governing equations were tackled with suitable similarity approach and then solved numerical using bvp-5c approach. The analysis was carried out in two different cases: i) with nanoparticle aggregation and ii) without nanoparticle aggregation to illustrate natural heat and mass transfer behavior. The key findings obtained in this work are addressed as follows:

1. Radial velocity and tangential velocity profiles increases but axial velocity profile drops for stretching ratio parameter.
2. Growing values of magnetic field reduces both radial and tangential velocity.
3. Augmented values of heat source/sink and Biot number enhance temperature profile.
4. Concentration profile reduces for reaction rate parameter while increases for activation energy.
5. Rise in horizontal magnetic field and stretching rate has boosted skin friction.
6. Augmentation in heat source/sink and Biot number has increased rate of heat transfer.
7. The rate of mass transfer rises for reaction rate parameter but drops for larger values of activation energy.

3.1 | Future Scope

Considering the results from the study, these results provide practical engineering perspectives of managing mass, heat, and momentum transfer in rotating disk systems. The results are especially applicable to thermal configuration and optimization of magnetically regulated reactors or rotating turbines systems, where efficient heat and mass transfer with boundary layer management are crucial.

Nomenclature

Symbols

$\vec{B}$	Uniform magnetic field (A/m)
Bi^*	Biot number
C	Concentration $(molm^{-3})$
C_w	Wall concentration $(molm^{-3})$
C_∞	Concentration at far field $(molm^{-3})$
Cf	Skin friction
Cp	Specific heat capacity $(m^2s^{-2}K^{-1})$

D	Diffusivity (m^2s^{-1})
E	Activation energy
E_a	Activation energy component (J)
F	Radial velocity profile
G	Tangential velocity profile
h_f	Convective heat transfer coefficient ($kgs^{-3}K^{-1}$)
H	Axial velocity profile
$\vec{J}$	Current density (Am^{-2})
k	Thermal conductivity ($kgms^{-3}K^{-1}$)
K	Boltzmann constant ($kgm^2s^{-2}K^{-1}$)
K_r^*	Reaction rate (s^{-1})
M	Magnetic field parameter
Nu	Nusselt number
p	Pressure term ($kgm^{-1}s^{-2}$)
P	Pressure profile
Q	Heat source/sink parameter
Q_0	Volumetric rate of heat source/sink ($kgm^{-1}s^{-3}K^{-1}$)
Rc	Chemical reaction parameter
Re	Reynolds number
S	Stretching ratio
Sc	Schmidt number
Sh	Sherwood number
T	Temperature (K)
T_w	Wall temperature (K)
T_∞	Temperature at far field (K)
$\{u,\ v, w\}$	Velocity components (ms^{-1})
$\{r,\ \varphi, z\}$	Cylindrical coordinates (m)

Greek Symbols

μ	Dynamic viscosity ($kgm^{-1}s^{-1}$)
υ	Kinematic viscosity (m^2s^{-1})
σ_e	Magnetic conductivity ($\Omega^{-1}m^{-1}$)
ρ	Density (kgm^{-3})
η	Similarity variable
γ	Angle of inclination
δ	Temperature difference ratio
Ω	Angular velocity (s^{-1})
θ	Temperature profile
χ	Concentration profile

Subscripts

f	base fluid
nf	nanofluid
agg	aggregation

Acknowledgements

Dr. Nihaal K.M., sincerely thanks the University of Tarapacá (Chile), for the kind invitation and generous hospitality extended to him as a visiting scholar through the Visiting Researchers Program during the academic year 2025-2026. He expresses his deep gratitude to his research supervisor, Professor U. S. Mahabaleshwar, for his constant guidance and support, and also extends sincere thanks to Prof. L. M. Pérez (Universidad de Tarapacá), for her warm hospitality and valuable assistance during his visit.

Funding

L.M.P. acknowledges partial financial support from FONDECYT (Grant ID 1240985) and Centres of Excellence with BASAL/ANID (CIA250002, CEDENNA).

Conflicts of Interest

The authors declare no conflicts of interest.

Data Availability Statement

Data is available from the corresponding author on reasonable request.

References

1. K. Muhammad, M. Sarfraz, H. F. Alrihieli, and I. E. Elseesy, “Significance of Brownian Diffusion and Thermophoresis in Energy and Mass Optimization for Newtonian and Non-Newtonian Fluid Flow: A Numerical Study via Keller-Box method,” *Case Studies in Thermal Engineering* 72 (2025): 106365, https://doi.org/10.1016/j.csite.2025.106365.

2. A. Mishra, “Hydrothermal Performance of Hybrid Nanofluid Flow Over an Exponentially Stretching Sheet Influenced by Gyrotactic Microorganisms: A Comparative Evaluation of Yamada-Ota and Xue Models,” *Numerical Heat Transfer; Part A: Applications* 86, no. 24 (2025): 8817–8846, https://doi.org/10.1080/10407782.2024.2363496.

3. K. Muhammad, M. Sarfraz, N. A. Ahammad, and I. E. Elseesy, “Improving Thermal Efficiency Through Cu-MoS_2 Hybrid Nanomaterials: A Numerical and Statistical Approach,” *Chaos, Solitons & Fractals* 192 (2025): 116014, https://doi.org/10.1016/j.chaos.2025.116014.

4. K. M. Nihaal, U. S. Mahabaleshwar, N. Swaminathan, and G. V. Bognar, “Optimization of Heat Transfer Analysis on an Aggregated Nanofluid Flow Over a Thin Porous Needle: Sensitivity Analysis Approach,” *International Journal of Thermofluids* 27 (2025): 101191, https://doi.org/10.1016/j.ijft.2025.101191.

5. M. Waseem, W. H. Hassan, M. Jawad, G. Bognár, and R. Ghodhbani, “Examination of Chemical Reaction on Second-Grade Nanofluid and Micropolar Nanofluid due to Exponential Stretchable Sheet: A Comparative Study,” *South African Journal of Chemical Engineering* 53 (2025): 373–385, https://doi.org/10.1016/j.sajce.2025.05.010.

6. M. M. Bhatti, R. Ellahi, and S. M. Sait, “Numerical Investigation of Magnetized Nanofluid Flow in a Non-Darcian Medium With Convective Heating Conditions Across a Rotating Disk,” *International Journal of Numerical Methods for Heat and Fluid Flow* 35, no. 5 (2025): 1736–1763, https://doi.org/10.1108/HFF-03-2025-0135.

7. M. Sarfraz, K. Muhammad, N. A. Ahammad, and I. E. Elseesy, “Synergistic Effects of Cadmium Telluride and Graphite Nanoparticles With Entropy Analysis Through Keller-Box Method,” *International Communications in Heat and Mass Transfer* 163 (2025): 108667, https://doi.org/10.1016/j.icheatmasstransfer.2025.108667.

8. K. Muhammad and M. Sarfraz, “Regression Analysis of Squeezing-induced Hybrid Nanofluid Flow in Darcy–Forchheimer Porous Medium,” *Applied Mathematics and Mechanics* 46, no. 1 (2025): 193–208, https://doi.org/10.1007/s10483-025-3202-9.

9. S. Mandal, S. Mukherjee, G. C. Shit, and K. Vajravelu, “Entropy Analysis of MHD Flow in Hybrid Nanofluid Over a Rotating Disk With Variable Viscosity and Nonlinear Thermal Radiation,” *ZAMM—Journal of Applied Mathematics and Mechanics (Zeitschrift für Angewandte Mathematik und Mechanik)* 105, no. 2 (2025): e202301027, https://doi.org/10.1002/zamm.202301027.

10. M. Turkyilmazoglu, “Flow and Heat Over a Rotating Disk Subject to a Uniform Horizontal Magnetic Field,” *Zeitschrift für Naturforschung A* 77, no. 4 (2022): 329–337, https://doi.org/10.1515/zna-2021-0350.

11. S. A. Shehzad, A. Rauf, B. Perveen, et al., “Numerical and Regression Analysis of Horizontal Magnetic Field in Slippery Nanofluid Flow With Arrhenius Activation Energy,” *Journal of Molecular Liquids* 392 (2023): 123522, https://doi.org/10.1016/j.molliq.2023.123522.

12. A. K. Pandey and A. Das, “Thermohydrodynamics of Bödewadt Hybrid-nanofluid Flow in a Horizontal Magnetic Field,” *European Journal of Mechanics - B/Fluids* 106 (2024): 148–165, https://doi.org/10.1016/j.euromechflu.2024.04.011.

13. M. Awais, S. Bilal, and M. Y. Malik, “Numerical Analysis of Magnetohydrodynamic Navier’s Slip Visco Nanofluid Flow Induced by Rotating Disk With Heat Source/Sink,” *Communications in Theoretical Physics* 71, no. 9 (2019): 1075, https://doi.org/10.1088/0253-6102/71/9/1075.

14. S. Kumar and K. Sharma, “Darcy-Forchheimer Fluid Flow Over Stretchable Rotating Disk Moving Upward/Downward With Heat Source/Sink,” *Topics & Reviews in Porous Media: An International Journal* 13 (2022): 33–43, https://doi.org/10.1615/SpecialTopicsRevPorousMedia.2022043951.

15. M. Sarfraz, K. Muhammad, H. F. Alrihieli, and M. A. H. Abdelmohimen, “Heat and Mass Transfer Analysis in Flow of Walter’s B Nanofluid: A Numerical Study of Dual Solutions,” *ZAMM—Journal of Applied Mathematics and Mechanics / Zeitschrift für Angewandte Mathematik und Mechanik* 105, no. 1 (2025): e202300951, https://doi.org/10.1002/zamm.202300951.

16. K. M. Nihaal, U. S. Mahabaleshwar, and S. W. Joo, “Darcy Forchhiemer Imposed Exponential Heat Source-sink and Activation Energy With the Effects of Bioconvection Over Radially Stretching Disc,” *Scientific Reports* 14, no. 1 (2024): 7910, https://doi.org/10.1038/s41598-024-58051-5.

17. U. Farooq, M. Imran, S. Noreen, N. Fatima, and T. Muhammad, “Heat Transfer Performance of Hybrid Nanofluid Radiative Flow via a Rotating Disk With Heat Source–Sink Effects and Response Surface Methodology,” *Mathematicsl Methods in the Applied Sciences* (2025), https://doi.org/10.1002/mma.10821.

18. H. Arafat, F. Ali, N. A. Shah, M. O. Sidi, and S.-J. Yook, “Theoretical Analysis of Activation Energy of Darcy–Forchheimer Fractional Bioconvection Flow of Nanofluid due to a Rotating Disk With Entropy Generation,” *Fractals* 33, no. 10 (2025): 2540247, https://doi.org/10.1142/S0218348X25402479.

19. S. A. M. Alsallami, H. Zahir, T. Muhammad, A. U. Hayat, M. R. Khan, and A. Ali, “Numerical Simulation of Marangoni Maxwell Nanofluid Flow With Arrhenius Activation Energy and Entropy Anatomization Over a Rotating Disk,” *Waves in Random and Complex Media* 35, no. 2 (2025): 2645–2663, https://doi.org/10.1080/17455030.2022.2045385.

20. A. Paul, B. Patgiri, and N. Sarma, “Mixed Convective Flow of Engine Oil-based Non-Newtonian Tri-hybrid Nanofluid Across a Porous Rotating Disk,” *World Journal of Engineering* 22, no. 3 (2024): 612–626, https://doi.org/10.1108/WJE-01-2024-0025.

21. G. A. Khouqeer, F. Haq, M. ur Rahman, and M. Sallah, “An Investigation of Thermo-bioconvective Ternary Hybrid Nanofluid Flow Over Rotating Disk Subject to Activation Energy,” *Journal of Thermal Analysis and Calorimetry* 150, no. 18 (2025): 14673–14685, https://doi.org/10.1007/s10973-025-14495-z.

22. M. Asma, W. A. M. Othman, T. Muhammad, F. Mallawi, and B. R. Wong, “Numerical Study for Magnetohydrodynamic Flow of Nanofluid due to a Rotating Disk With Binary Chemical Reaction and Arrhenius Activation Energy,” *Symmetry* 11 (2019): 1282.

23. D. Mohanty, G. Mahanta, S. Shaw, and R. Katta, “Entropy and Thermal Performance on Shape-based 3D Tri-hybrid Nanofluid Flow due to a Rotating Disk With Statistical Analysis,” *Journal of Thermal Analysis and Calorimetry* 149, no. 21 (2024): 12285–12306, https://doi.org/10.1007/s10973-024-13592-9.

24. A. Tulu, L. Asefa, and M. Sohail, “Unsteady Magnetohydrodynamic Hybrid Nanofluid Flow Over a Rotating Disk With Viscous Dissipation and Cattaneo–Christov Heat Flux Model,” *International Journal of Thermofluids* 21 (2024): 100586, https://doi.org/10.1016/j.ijft.2024.100586.

25. R. R. Meena and P. Sharma, “Thermal and Mass Diffusion in Chemically Reactive, Radiative Hybrid Nanofluid (Cu and TiO_2) Flow Over a Rotating Disk,” *International Journal of Thermofluids* 26 (2025): 101104, https://doi.org/10.1016/j.ijft.2025.101104.

26. P. Jalili, Z. Asadi, A. Shateri, et al., “Thermal Analysis of Nanofluid Magnetic Flow on a Rotating Disk in the Presence of Radiation Considering Response Surface Method,” *Modern Physics Letters B* 38, no. 24 (2024): 2450217, https://doi.org/10.1142/S0217984924502178.

27. A. M. Galal, A. Mabrouk, S. Liaqat, et al., “Radiation Effects on Thermo-bioconvection Flow of Trihybrid Nanofluid Through an Inclined Rotating Disk With Applications of the Cattaneo-Christov Flux Model,” *Journal of Radiation Research and Applied Sciences* 18, no. 1 (2025): 101293, https://doi.org/10.1016/j.jrras.2025.101293.

28. M. Sarfraz and K. Muhammad, “Modulation of Energy Transport in Stagnation Point Flows Involving Hybrid Nanofluids,” *Proceedings of the Institution of Mechanical Engineers, Part N: Journal of Nanomaterials, Nanoengineering and Nanosystems* (2025), https://doi.org/10.1177/23977914251322202.

29. K. Muhammad, M. Sarfraz, A. Ebaid, and H. Elmannai, “Optimization of Energy Transport via Electro-thermal Hybrid Nanofluid in Parallel Disks: A Keller-Box Simulation,” *Chaos, Solitons & Fractals* 198 (2025): 116621, https://doi.org/10.1016/j.chaos.2025.116621.

30. M. Sarfraz and K. Muhammad, “Numerical Solutions for Thermal and Solutal Transport of Jeffrey Fluid Flow Subject to Rotation via Keller–Box Method,” *Multiscale and Multidisciplinary Modeling, Experiments and Design* 8, no. 3 (2025): 177, https://doi.org/10.1007/s41939-024-00714-x.

31. R. Ellahi, M. Hassan, and A. Zeeshan, “Aggregation Effects on Water Base Al_2O_3—Nanofluid Over Permeable Wedge in Mixed Convection,” *Asia-Pacific Journal of Chemical Engineering* 11, no. 2 (2016): 179–186, https://doi.org/10.1002/apj.1954.